

Article

Characterization, Calcination and Pre-Reduction of Polymetallic Manganese Nodules by Hydrogen and Methane

Ole Kristian Brustad , Jonas Låstad, Arman Hoseinpur  and Jafar Safarian * 

Department of Materials Science and Engineering, Norwegian University of Science and Technology (NTNU), Alfred Getz Vei 2, 7034 Trondheim, Norway

* Correspondence: jafar.safarian@ntnu.no; Tel.: +47-48061765

Abstract: A polymetallic manganese nodule was characterized and further calcined and pre-reduced by H₂, CH₄, and H₂-CH₄ mixtures at elevated temperatures. It was found that the main Mn and Fe elements coexisted in the ore in different minerals, and the Mn/Fe ratio varies in the ore. Moreover, Cu, Ni and Co are distributed with Mn and Fe, and no known minerals of these elements were identified. The calcination of the ore was carried out through calcination in air in a muffle furnace, and under Ar in a thermogravimetry (TG) furnace. It was found that manganese and iron oxides are evolved from a variety of oxide and hydroxides in the ore during calcination. The pre-reduction of the calcined ore particles by H₂ gas in the TG furnace indicated fast reduction by hydrogen. The pre-reduction of the calcined ore by H₂, CH₄, and H₂-CH₄ mixtures in a stationary bed reactor and further characterization of the products indicated the same products. It was found that the pre-reduction by all the applied gases at elevated temperatures yield a pre-reduced ore that contains metallic Fe, Cu, Ni, and Co, while MnO co-exist as the dominant phase.



Citation: Brustad, O.K.; Låstad, J.; Hoseinpur, A.; Safarian, J. Characterization, Calcination and Pre-Reduction of Polymetallic Manganese Nodules by Hydrogen and Methane. *Metals* **2022**, *12*, 2013. <https://doi.org/10.3390/met12122013>

Academic Editors: Pasquale Cavaliere, Geoffrey Brooks and Carlos Capdevila-Montes

Received: 19 August 2022

Accepted: 18 November 2022

Published: 24 November 2022

Publisher's Note: MDPI stays neutral with regard to jurisdictional claims in published maps and institutional affiliations.



Copyright: © 2022 by the authors. Licensee MDPI, Basel, Switzerland. This article is an open access article distributed under the terms and conditions of the Creative Commons Attribution (CC BY) license (<https://creativecommons.org/licenses/by/4.0/>).

Keywords: manganese nodules; calcination; hydrogen; methane; pre-reduction; thermogravimetry; iron; copper; nickel; cobalt

1. Introduction

The major shift towards sustainable development is causing further strain on material supply. The adoption of battery technology, electrification, digitalization, and advanced materials places new and increased demands for material value chains. According to Halada et al., the projected demand for several metals will outstrip existing reserves or even reserve bases for several key metals [1]. This highlights the need to increase the use of recycling as well as the exploration of potential reserves. Polymetallic manganese nodules (PMMN) have been explored as possible reserves for metals such as Mn, Cu, Ni, and Co that can respond to the forthcoming challenges for raw material supply [2].

Polymetallic manganese nodules are rock concretions of subsea minerals due to their formation mechanisms and contain useful amounts of various valuable metals [3]. These metals exist as metal oxides formed by hydrogenetic and diagenetic precipitation on the sea floor. These minerals occur on the sea floor in all major oceans, but in high quantities in areas such as the Clarion-Clipperton Fracture Zone, Cook Island, Peru Basin, and Indian Ocean at depths between 4000 and 6000 m [3]. The extraction of valuable metals from PMMN can be performed in multiple different extraction processes, but a common factor is the reduction of the minerals [4,5]. A variety of techniques have been applied in the lab scale to process PMMN, as has been reviewed recently [6]. These techniques can be classified as hydrometallurgical, pyrometallurgical, or their combinations. In the pyrometallurgical processes, however, reductive roasting and carbothermic reduction-smelting have been studied [7–9]. The hydrogen roasting reduction indicated that the reactions in the ore occur in the sequence of water evaporation, decomposition of hydroxides, the reduction of Cu, Ni, and Co oxides, and then Fe oxides reduction [7]. The move towards decarbonization

introduces new challenges to the metallurgical field of pyrometallurgy, and those must be considered in future processes that are applied for PMMN processing. Hydrogen and methane are important as a substitution to coal and metallurgical coke as reduction agents, which vastly reduces the carbon footprint [10–12]. The application of hydrogen and natural gas instead of solid carbon materials (metallurgical coke) as the reductant is accompanied with less CO₂ emissions and is, in principle, more sustainable.

The objective for this research is to perform a series of reduction experiments utilizing different atmospheres consisting of methane and hydrogen gases. The characterization of PMMN is performed, as well as the calcined and reduced ore, to gain insight into the mechanisms of reduction of the PMMN. The characterization techniques utilized in this paper are chemical analysis through X-ray fluorescence (XRF), phase analysis through X-ray diffraction (XRD) and microstructural analysis through scanning electron microscope (SEM). An ideal result of this research is to contribute to the research field and build valuable knowledge for the possible seafloor minerals processing, as well as contributing to decarbonization in the metallurgical processes.

2. Materials and Methods

2.1. Raw Material and Preparation

A PMMN from the Clarion-Clipperton Fracture Zone was used in the present work. A portion of the ore sample was crushed into a fine powder for analysis by XRD and XRF. The rest of the ore was crushed and sized to the particle size of 4–10 mm for further studies, and this particle size range was used to have more homogeneous samples in the calcination and reduction experiments.

2.2. Calcination

The calcination of the ore was performed for 2 h at 1173 K with a heating rate of 20 K/min to this temperature in a muffle furnace (Nabertherm GmbH, Lilienthal, Germany) in exposure to air and under a fume hood. A smaller batch of 2.14 g was put in an alumina container and calcined using a thermogravimetry setup (Linseis STA PT1600 thermal analyzer, Linseis Messgeräte GmbH, Robbinsville, NJ, USA) for 1 h at 1173 K with a heating rate of 5 K/min to this temperature to study the mass changes upon heating. The selected temperature and durations were based on the literature survey and calcination behavior of manganese ores as reviewed by Cheraghi et al. [12].

2.3. Reduction by Hydrogen and Methane

2.3.1. Hydrogen Reduction Using Thermogravimetry

The hydrogen reduction using the above mentioned thermogravimetry furnace was performed on a sample of 1.79 g. The sample was heated to 1173 K from room temperature at a rate of 10 K/min, the selection of 10K/min was due to the results of the calcination study and having the possibility of complete calcination with this rate prior to hydrogen introduction at the target temperature. During heating and cooling a gas flow of 0.2 NL/min of Ar was used, while at the working temperature, a gas flow of 0.2 NL/min of H₂ was used. Due to the risk of methane cracking at elevated temperatures, causing damage to the instrument, only hydrogen reduction was used for TGA.

2.3.2. Reduction in a Stationary Bed Reactor

The reduction experiments were performed in a vertical tube resistance furnace (Thermal Technology LLC, Minden, NV, USA), and the details of the reactor were described previously [13]. The reduction experiments were carried out under 4 different gas compositions. The gas compositions used are given in Table 1 together with the initial ore sample weight and the reduction temperature. Gas introduction to the sample bed was done from beneath an alumina mesh so that a uniform gas moved upwards through the bed. The experiment with 100% H₂ was performed at 1288 K, while the other experiments, containing methane, were performed at 1133 K. Prior to heating, the furnace was flushed by argon,

evacuated, and flushed to atmospheric pressure with argon. The samples were heated for 30 min in a gas flow of 2 NL/min Ar and the reduction was performed for 90 min with a total gas flow rate of 2 NL/min. Cooling was performed under a 2 NL/min Ar for 50 min before the furnace was turned off. When the sample reached room temperature the furnace was flushed and purged with argon again before extracting the samples. The selected gas compositions were based on introducing H₂ (exp 1) and CH₄ (experiment 4) with a similar number of moles of hydrogen in these two experiments, while in the mixtures of experiments 2 and 3 we tried to have mixtures of CH₄ and H₂ with a significant difference in hydrogen content.

Table 1. The reduction conditions in the stationary bed reactor.

Experiment	Ar/CH ₄ /H ₂ [vol%]	Sample Weight [g]	Temperature [K]
1	0/0/100	49.72	1288
2	10/50/40	50.19	1133
3	40/50/10	49.18	1133
4	50/50/0	50.41	1133

2.4. Characterization Techniques

Powder samples of the raw, calcined, and reduced ore were prepared via milling in a ring mill (Fritsch GmbH, Idar-Oberstein, Germany) for XRD and XRF analysis. Phase analysis by XRD was performed with a speed of 1° per minute between 10° and 90° diffraction angle using a Rigaku MiniFlex 600 (Malvern, UK), with Cu-K α radiation. The raw data from the XRD was analyzed using EVA software (version 6, Bruker AXS, Madison, WI, USA) using the databases PDF-4+ and COD. Chemical analysis by XRF was performed by Degerfors Laboratorium AB (Degerfors) in Sweden. Microstructural analysis the sample particles were carried out in a scanning electron microscope (SEM) (Zeiss, Oslo, Norway). The samples were imaged using backscattered electrons. EDS-mapping by SEM were performed to collect data on elements distribution. Prior to being examined, the samples were cast in resin, ground down up to 4000 grit paper and coated via sputtering of gold or glow discharge of carbon. The raw and calcined samples were coated using carbon, while the reduced samples were coated with gold.

3. Results

3.1. Characteristics of the Ore

During crushing, white particles of various sizes were discovered as inclusions in the ore. These particles could be liberated from the ore and analyzed. Figure 1 shows the received pre-crushed ore particles before further crushing in this study. It was found in the ore particles that there is inhomogeneity and small bright particles are distributed in a dark matrix, as seen in Figure 1a,b. In addition, some small bright particles were later found in the crushed ore particles, as shown in Figure 1c. Obviously, the material has high inhomogeneity from particle to particle.

3.1.1. Chemical Analysis (XRF)

Chemical composition analysis of the raw and calcined PMMN by XRF measurements are given in Table 2. The received XRF results were normalized to replace the MnO phase for the raw ore with MnO₂ and with Mn₂O₃ for the calcined ore (considering XRD results that are presented later). The LOI for the raw ore was determined to be 15.4%, the loss from drying at 353 K (mostly free moisture) overnight was subtracted from the average loss from calcination. The XRF data from the supplier presents Ni, Cu, Co, and Ba in their metallic phases.

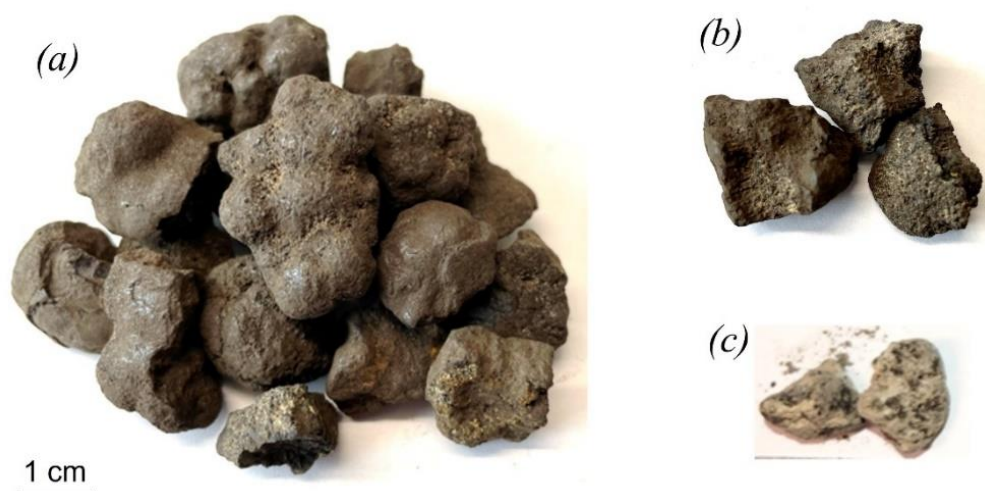


Figure 1. (a,b) Visual illustration of the received PMMN particles, and (c) separated bright particles.

Table 2. XRF analysis from supplier and measurements in this study.

Element	Raw (Supplier)	Raw (Measured)		Calcined (Measured)	
	(wt%)	(wt%)	Normalized(wt%)	(wt%)	Normalized (wt%)
CaO	2.22	3.45	2.95	3.05	2.89
MgO	3.44	3.83	3.28	4.96	4.71
SiO ₂	17.92	34.6	29.60	16.2	15.37
Al ₂ O ₃	6.73	12.1	10.35	6.73	6.39
Fe ₂ O ₃	4.18	7.00	5.99	8.84	8.39
Mn _x O _y *	40.03	23.3	24.43	48	50.69
Cr ₂ O ₃	-	0.02	0.02	-	-
V ₂ O ₅	-	0.05	0.04	0.1	0.09
TiO ₂	0.38	0.87	0.74	0.68	0.65
NiO	1.00	1.14	0.98	2.4	2.28
Na ₂ O	-	2.57	2.20	3.29	3.12
K ₂ O	-	2.56	2.19	1.26	1.20
P ₂ O ₅	-	0.41	0.35	0.39	0.37
SO ₃	-	0.11	0.09	0.22	0.21
ZnO	-	0.11	0.09	0.29	0.28
MoO ₃	-	0.01	0.01	0.1	0.09
CuO	1.00	0.84	0.72	1.72	1.63
PbO	-	-	-	0.06	0.06
ZrO ₂	-	0.01	0.01	0.03	0.03
SrO	-	0.05	0.04	0.08	0.08
BaO	0.3	0.20	0.17	0.28	0.27
Cl	-	0.22	0.19	0.03	0.03
Co ₃ O ₄	0.2	0.17	0.15	0.36	0.34
CeO ₂	-	0.01	0.01	-	-
Y ₂ O ₃	-	-	-	0.03	0.03
LOI	-	6.26	15.4	0.81	0.81

* Mn_xO_y is presented as MnO in the non-normalized values, as MnO₂ in the normalized raw ore, and as Mn₂O₃ in the normalized calcined ore.

3.1.2. Phase Analysis (XRD)

The XRD analysis result for the raw ore is shown in Figure 2 and it indicates that the ore contains quartz (SiO₂), albite (NaAlSi₃O₈), goethite (α -FeO(OH)), Ca-Mg-Si (CaMgSi₂O₆), asbolane (NiMn₂O₃(OH)₄·H₂O), lithiophorite (Al_{0.65}H₂Li_{0.33}MnO₄), manganese oxide (MnO₂), vernadite (Mn(OH)₄), chalcophanite (H₆Mn₃O₁₀Zn), and birnessite (MnO₂). A lot of noise in the diffraction pattern was observed, which makes phase identification challenging.

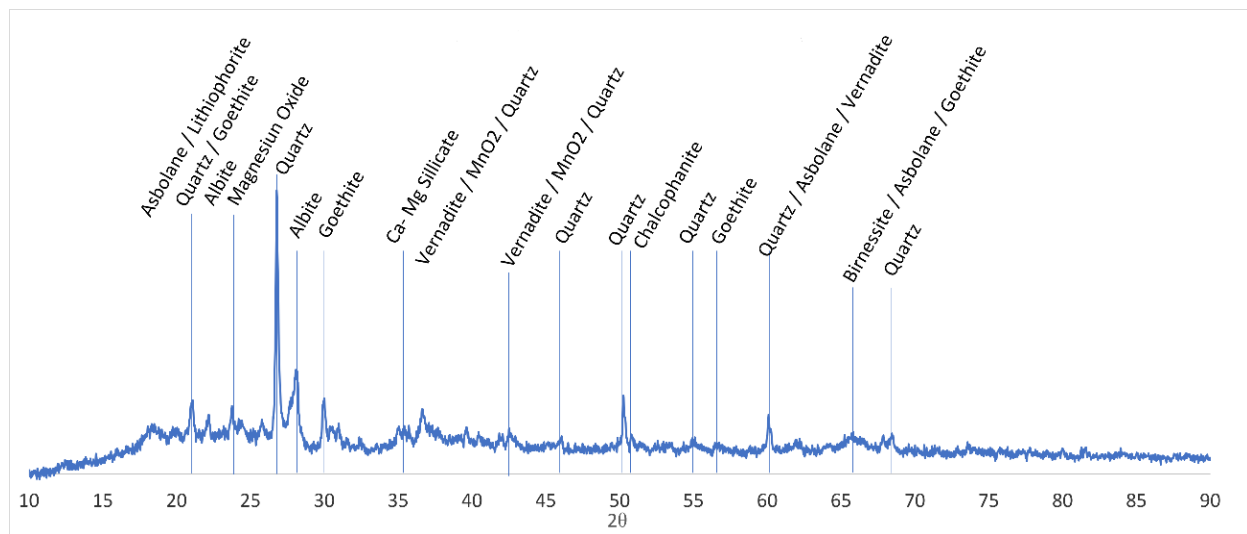


Figure 2. XRD pattern of a raw PMMN with identified peaks.

The bright particles found in the nodules (Figure 1c) were collected and analyzed using XRD. The resulting XRD spectrum is shown in Figure 3 to assess the contained phases. The main phases identified were quartz (SiO_2), and albite ($\text{NaAlSi}_3\text{O}_8$), and the ore contains minor amounts of phlogopite ($\text{KMg}_3(\text{Si}_3\text{Al})\text{O}_{10}(\text{OH})_2$) and MgAl_2O_4 spinel. Hence, the bright particles were mostly silica and silicates, which are without valuable Mn, Ni, Cu and Co metals.

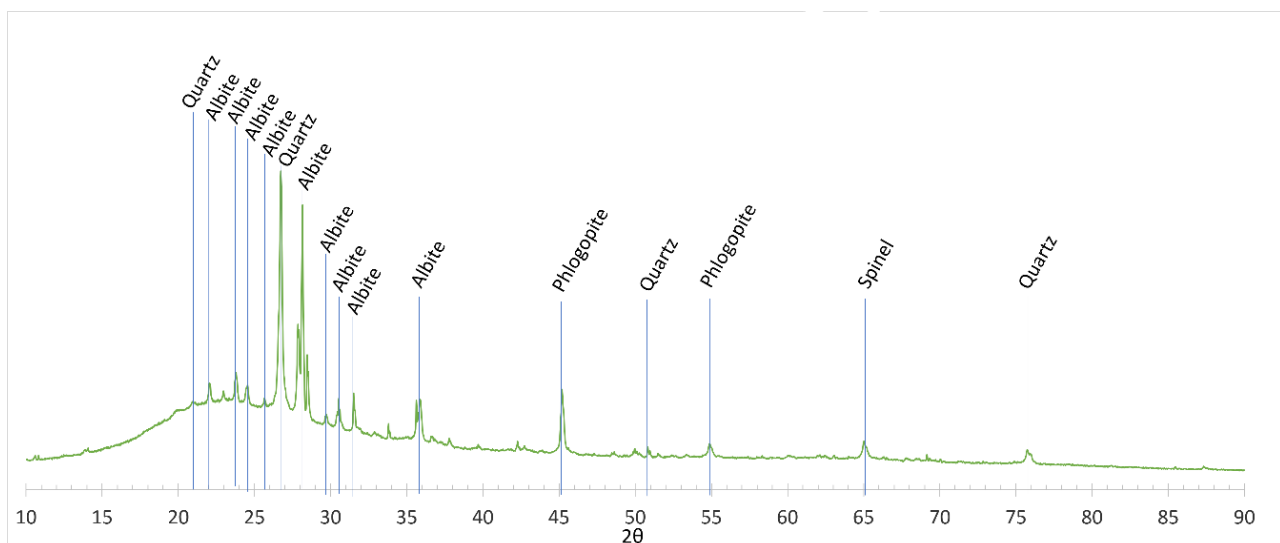


Figure 3. XRD pattern of liberated white particles in the raw PMMN with identified peaks.

3.1.3. Microstructural Analysis

A typical SEM image of a raw PMMN in Figure 4 shows a fine layered structure, and the ore obviously has some porosity and chemical inhomogeneity as the back-scattered image (BSI) illustrates. It is worth mentioning that the material was relatively soft compared to onshore Mn ores and it was challenging to prepare the SEM metallography sample.

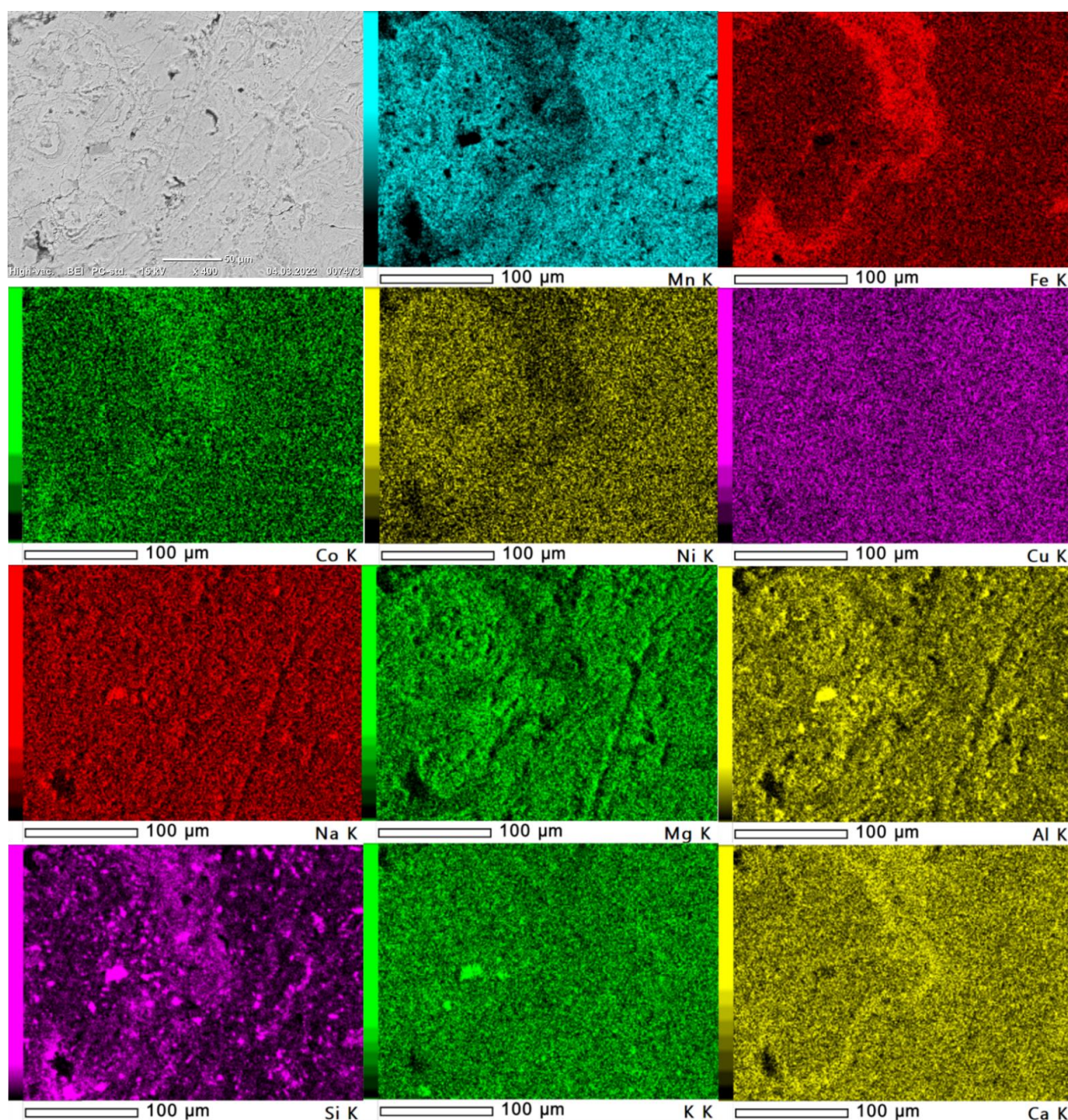


Figure 4. SEM-BEI image of the raw ore and elemental distribution mapping by EDS of the same area.

3.2. Calcination and Reduction Behavior of the Ore

3.2.1. Mass Changes

The average mass changes were calculated for calcination and reduction using the measured mass data for different samples. Table 3 shows the mass and percentage mass losses for the calcination in crucibles. For the calcination, the average weight loss was found to be approximately 27.3%, correlating well with the data from the thermogravimetry, which found a mass loss of 27.1%.

The TG diagram for the calcination of raw ore in Figure 5 shows that a rapid mass loss occurred at around 373 K, and the rate of mass loss slows down before making another step around 673 K, and again at 823 K. No more significant mass change was measured beyond 1073 K. The total mass loss measured at the end of the TG experiment was approximately 578 mg. The relative mass loss is a more useful value for comparison and is calculated to

be approximately 27.1%. Hence, there is a good correlation between the data in Table 3 and Figure 5.

Table 3. Mass data and mass losses in calcination of the raw PMMN ore.

Sample	Mass Before [g]	Mass After [g]	Mass Loss [g]	Mass Loss [wt%]
Crucible 1	37.52	27.09	10.42	27.8
Crucible 2	84.57	61.34	23.23	27.5
Crucible 3	26.83	19.48	7.35	27.4
Crucible 4	169.45	123.25	46.20	27.3
Crucible 5	170.21	124.05	46.16	27.1
Sum	488.58	355.21	133.37	27.3

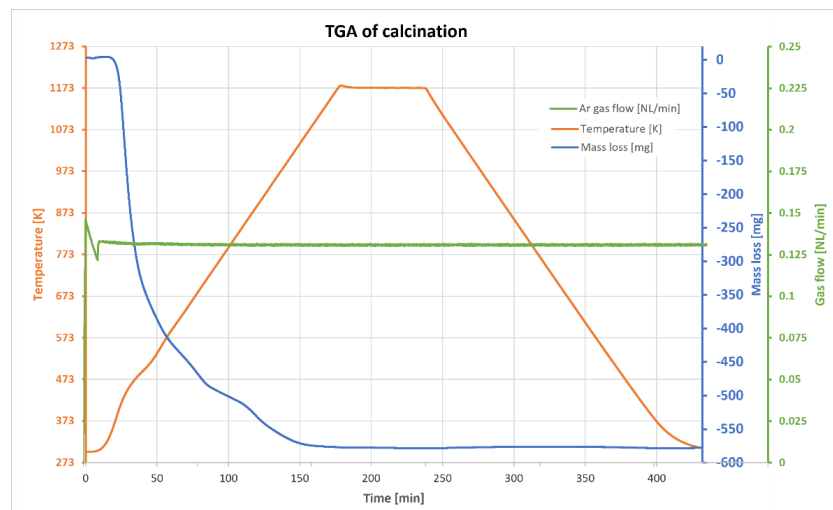


Figure 5. Thermogravimetric analysis from the calcination process of the raw PMMN.

The TG analysis with hydrogen introduction in Figure 6 shows a sharp mass loss when hydrogen was introduced to the pre-calcined sample, and the rate of mass loss quickly slowed down within about 20 min after hydrogen purging. At the point where the sample began cooling and the hydrogen supply was stopped, the curve was disturbed, after which the mass loss appeared to accelerate. The final mass loss was measured to be 136 mg or 7.6%.

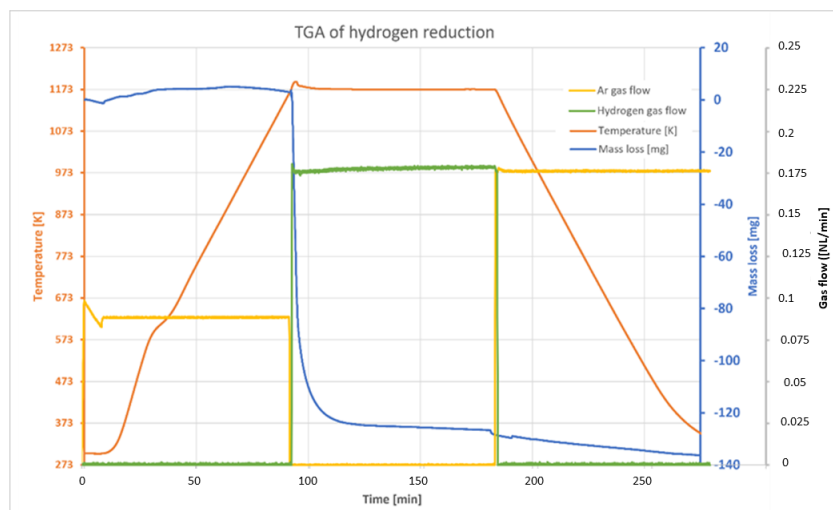


Figure 6. Thermogravimetric analysis of the reduction process with a 100% H₂ atmosphere of the calcined ore from the previous TGA.

Table 4 shows the mass data for the reduction experiments in the stationary bed reactor. The measured mass loss for the experiment with 100% H₂ gas is in good correlation with the TG test result in Figure 6. However, Table 4 shows that when methane or methane–hydrogen mixtures are used there is lower mass losses.

Table 4. Mass data and mass losses in reduction of calcined PMMN ore.

Sample	Mass Pre [g]	Mass Post [g]	Mass Loss [g]	Mass Loss [wt%]	Temperature [K]
100% H ₂	49.72	45.58	4.14	8.33	1288
50%CH ₄ 40%H ₂	50.19	48.02	2.17	4.32	1133
50%CH ₄ 10%H ₂	49.18	47.26	1.92	3.90	1133
50%CH ₄	51.41	46.47	3.94	7.82	1133

3.2.2. Phase Changes

The XRD spectrum of the calcined ore is shown in Figure 7. The peaks identified were manganese bearing magnetite ((Mn,Fe)₃O₄), bixbyite (Mn₂O₃), manganese oxide (ζMn₂O₃), and cuprite (Cu₂O). In the diffraction angle between 32.5° and 35°, there is overlapping of many peaks, and hence a band is seen instead of sharp peaks in this range. A few peaks were also not identified, such as the peaks at 36°, 58°, and 61°, after checking the databases with all the present elements found by XRF.

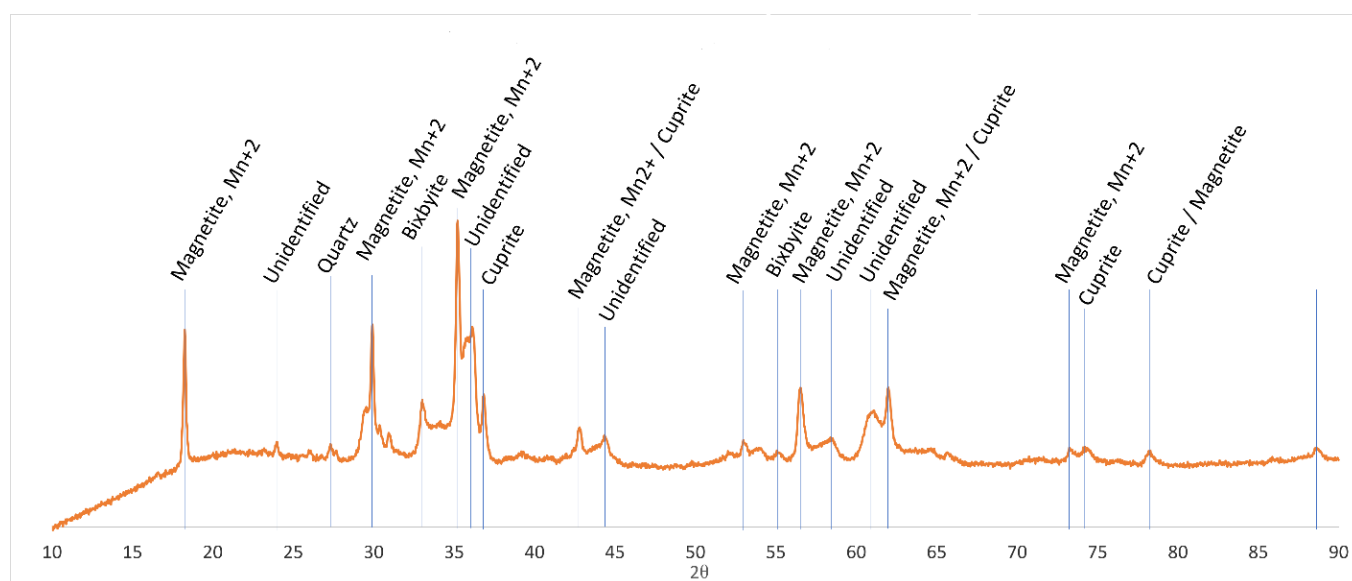


Figure 7. The XRD pattern of calcined PMMN with the identified peaks.

The XRD analysis of all the reduced samples with different gas compositions are presented in Figure 8. The diffraction patterns of the different samples are similar with the same identifiable phases. The identified phases were tephroite/fayalite((Fe,Mn)₂SiO₄), nepheline ((Na,K)AlSiO₄), manganosite (MnO), ferrite (α-Fe), and copper nickel (CuNi). Austenite (γ-Fe) and quartz (SiO₂) were only identifiable in the sample reduced in an atmosphere of 40% Ar, 50% CH₄, and 10% H₂.

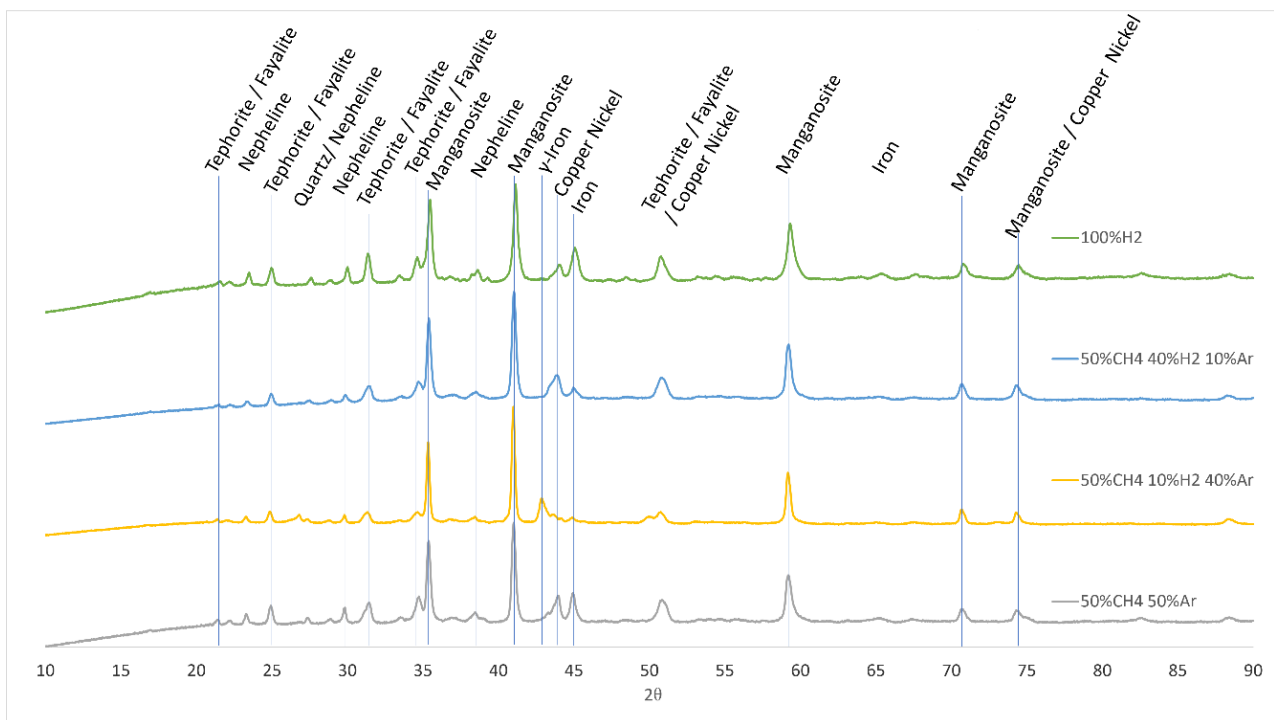


Figure 8. The stacked XRD patterns of PMMN samples reduced by different gases with their identified peaks.

3.2.3. Microstructural Changes

A typical SEM image of a calcined PMMN in Figure 9 shows a large pore volume evolution due to calcination. Obviously, there is less visible layered structure than that observed in the raw ore (Figure 4). Figure 9 also shows the distribution of the elements in different phases by BEI and elemental EDS mapping and have correlation with the observations in the ore.

A typical SEM image of a reduced PMMN particle in Figure 10 (experiment under a 50% Ar, 50% CH₄ atmosphere) is shown, which is representative for all the reduced samples. In comparison with the calcined sample, it has higher porosity, and the evolution of a fine porosity is obvious during the reduction.

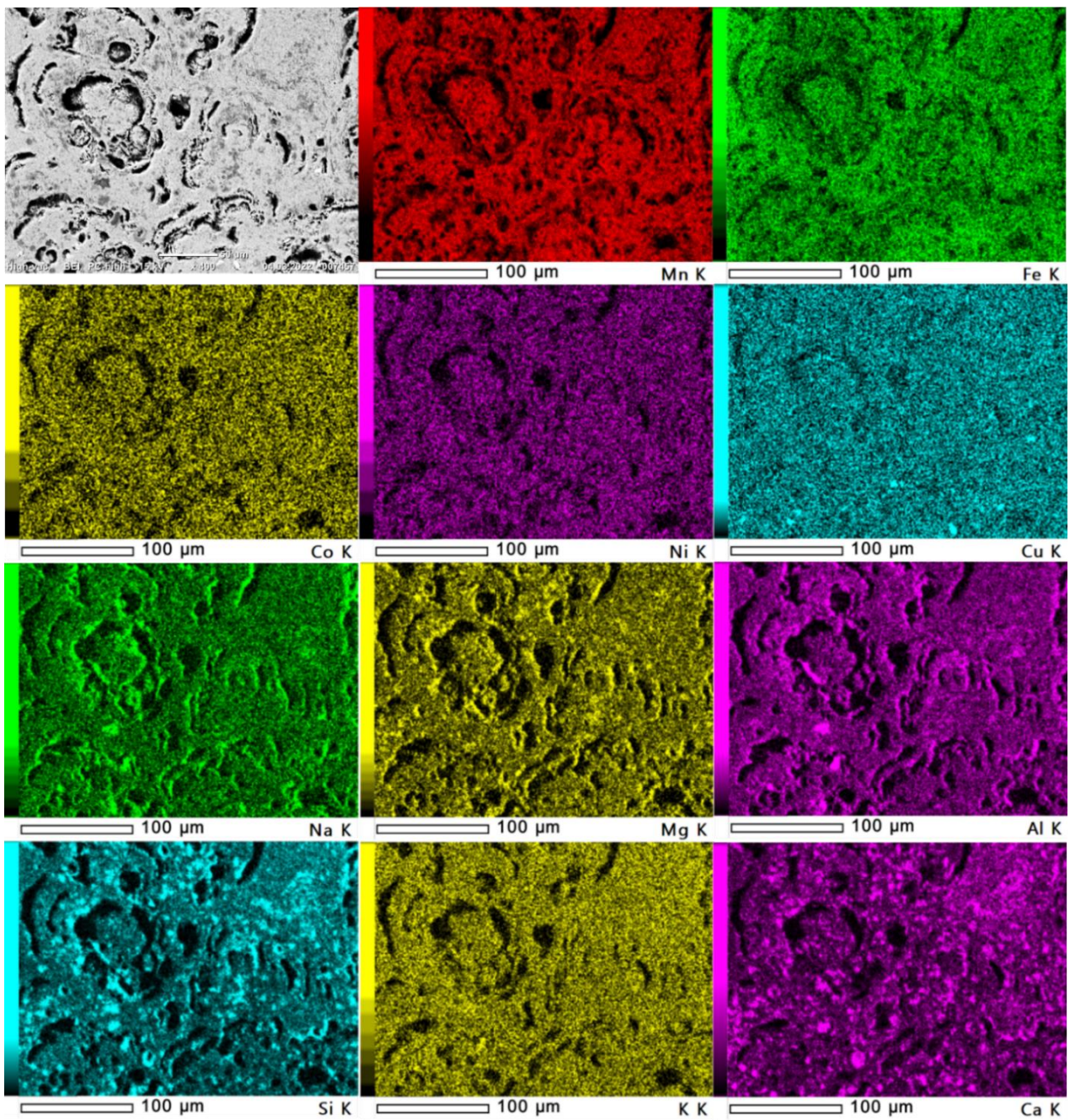


Figure 9. SEM-BEI image of the calcined ore and elemental distribution mapping by EDS of the same area.

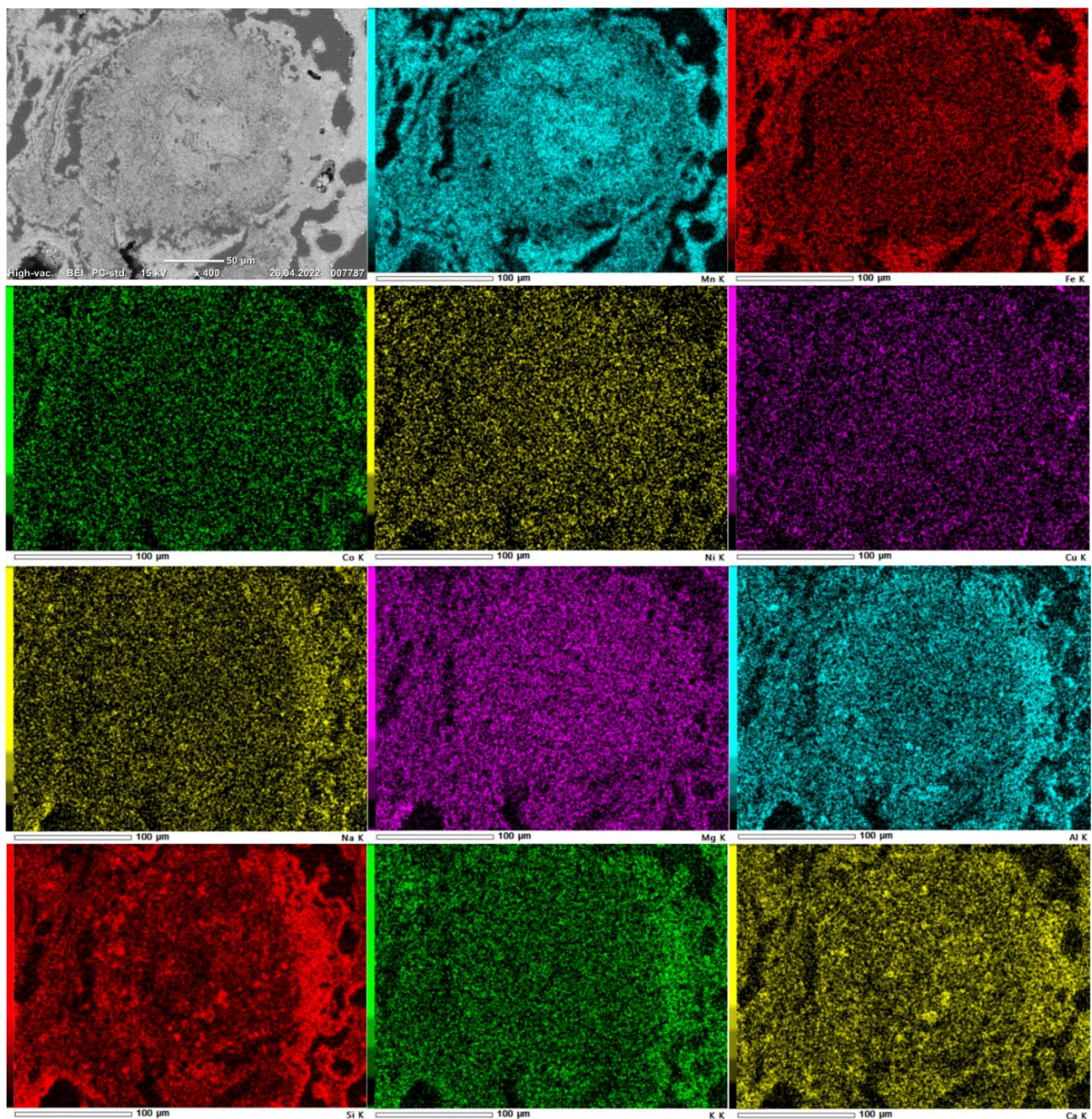


Figure 10. SEM-BEI image of a reduced PMMN and EDS elemental distribution mapping of the same area.

4. Discussion

4.1. Raw Ore Characteristics

The XRF results from the raw ore presented in Table 2 show a high amount of silicon in the ore, and the XRD pattern in Figures 2 and 3 show that it is mainly in the form of quartz. The high amount of silicon is not supported by the literature data, and the XRF results of the calcined sample in Table 2, which is lower, yet considerably above the literature data [3]. The high silicon content in the raw ore is most likely due to the inhomogeneities in the ore and the chance that the milled sample from the raw ore had, by chance, a higher amount of the white particles shown in Figure 1. The XRD pattern of these white particles in Figure 2 showed that the main elements in them are quartz and albite, and therefore they indicated higher Si content in the XRF analysis in Table 2. The received PMMN for this

study was a small batch and unfortunately it was not possible to study the overall average composition more precisely. The supplier, however, provided an XRF analysis, as given in Table 2. We expect to see some gangue due to the SiO_2 and Al_2O_3 content, the amount of other important metal oxides of Mn, Fe, Ni, Cu and Co in all XRF data are close and reliable. Hence, we may conclude that their elements are more homogeneously distributed in the ore.

Through the SEM study of the raw ore, as in Figure 4, only one phase was found to be easily identifiable. Through the EDS mapping this phase was identified to consist of Na, Si, Al, and K. However, this phase was not identified in the XRD results, as shown in Figure 2. Albite has the chemical formula $\text{NaAlSi}_3\text{O}_8$, and potassium can replace up to 10% of sodium in albite, which may explain this phase [14]. The XRF results, however, do not support that all the potassium resides in this phase. The EDS mapping also shows that aluminum occurs together with silicon, but this phase was not identified in the XRD. Silicon also occurs in other areas, which is mostly in quartz. Another observation from the EDS mapping is that manganese and iron reside in different phases, even though the pattern depicted in the mapping is not visible in the SEM image due to the very close atomic mass of Mn and Fe as 54.94 g/mol and 55.85 g/mol, respectively. In the EDS mapping in Figure 3, no quartz is observed as in this area it is not present. The distribution of Ni, Cu, and Co all over the sample indicate that they are not distributed in specific main minerals and their separation via mineral processing techniques is impossible or difficult [15]. Considering Fe distribution, we find out that it is associated with Mn; however, in some areas, the Mn/Fe ratio is higher, and, in some areas, lower than unity.

4.2. Phase and Structural Changes in Calcination

The diffraction pattern of the calcined ore in Figure 7 shows the presence of a wide band of increased intensity between multiple peaks between 32.5° and 35° angles. A possible explanation for this could be incomplete mass transfer during the calcination. This might also explain why the highest peak was found to be manganese bearing magnetite if the manganese is spread over several smaller peaks. Several of the peaks in the XRD pattern are wide and are possibly hiding smaller peaks beneath them. The widening of these peaks may be caused by an inhomogeneous strain because of the ore shrinking during calcination [16]. The association of Mn and Fe as two main components and observing their compositions profiles by EDS mapping in the ore may also be a reason for the obtained XRD result. There are solid solubilities between their oxides [17] and it is possible that many diffractions are obtained from different compositions of these oxides that yields the band in the XRD spectrum. This is supported by observing variations in Fe and Mn distributions in both the raw ore and calcined ore in the locations that they are present. Furthermore, in the XRD pattern there are some unidentified peaks, the main being at 44° , 58° , and 61° . The elements expected to be found here are Mg, Al, Si, Ca, and Ni. Comparing the EDS mapping of the raw ore in Figure 4 with the EDS mapping of the calcined ore in Figure 9, it is evident that manganese has moved from being prominent in some areas in the raw ore to being more evenly distributed throughout the calcined ore. However, maybe the applied time was not enough for their complete homogenization as the band in the XRD spectrum illustrates.

The TGA result in Figure 6 indicates several drops in the mass loss curve. The sharp drop of mass and further changes indicates gas evolution, and a leveling of the curve indicates a reaction ending [18]. The first sharp mass drop is found at approximately 373 K and can safely be assumed to be caused by the evaporation of free moisture and later hydroxides such as goethite. Hydroxides begin evaporating at higher temperatures, which may blur the contrast between the reactions at lower temperatures. The second identifiable mass drop occurs when the temperature reaches 673 K. At this temperature, SO_2 was detected using a handheld gas detector, and it is therefore assumed that this drop is caused by the decomposition of sulfides in the sample. The final mass drop occurs at

approximately 823 K and is assumed to be due to the partial reduction of Mn oxides via thermal decomposition and the decomposition of carbonates [19].

4.3. Reduction of Oxides

4.3.1. Gas Composition Effect

The reductions under a 100% H₂ and a 50% Ar, 50% CH₄ gases yielded very similar XRD patterns. This may indicate that the same reductions take place, and since there are no carbon available in the 100% H₂ and limited to no formation of carbides in the 50% Ar, 50% CH₄ atmosphere, we conclude that there are no differences between the different reduction atmospheres at 1133 K. The gas composition that stands out is the 40% Ar, 50% CH₄, 10% H₂, where it is believed that most of the iron has gone over into the γ -iron phase. Γ -iron is normally only stable at higher temperatures, but the presence of stabilizing elements such as manganese, cobalt, and nickel could have enabled the phase at room temperature [20]. In the XRD pattern of this sample, quartz was observed, and it might indicate that the analyzed sample had some quartz particles. However, as the peaks for nepheline, fayalite, and tephroite also are lower compared to the other samples it could be the result of fewer formations of these phases during the reduction step.

The similarities between the different gas mixtures can mainly be explained by the temperature. At 1133 K, methane and hydrogen are both able to perform the same reductions. While Fe, Co, Ni and Cu are reduced to metallic states at this temperature, this is not the case for Mn oxides, which are found in the state of MnO.

4.3.2. Products Characteristics

In the XRD analysis of the reduced samples, manganese was found in the state of manganosite, iron in the metallic form, and Cu and Ni, in elemental or Cu–Ni alloy form. The reduction to these states is expected as they are described in the literature [12]. Cu and Ni can easily form a solid solution with each other and may be hard to separately identify by XRD due to their low contents [21]. There is a homogeneous distribution of Ni and Cu in the ore and so the reduced ore may enhance such solid solution formation as short diffusion distances are needed for them to join. However, the amount of such alloy particles is small, and therefore we do not see specific XRD peaks of them in the reduced samples in Figure 7. Cobalt is also thermodynamically expected to be reduced to a metallic state; although, no cobalt was detected in the XRD analysis. Additionally, manganese and iron were found in the form of fayalite and tephroite, which are two species of olivine, with the chemical formulas Fe₂SiO₄ and Mn₂SiO₄, respectively. An intermediate phase between these two are knebelite, with the chemical formula FeMnSiO₄. The formation of fayalite is spontaneous under a reducing atmosphere at higher temperatures [22]. Given the similarities between fayalite and tephroite, it is also expected to be the case for the latter. Fayalite was identified in the samples reduced in 40% Ar, 50% CH₄, 10% H₂, and 10% Ar, 50% CH₄, 40% H₂ atmospheres, and tephroite in 100% H₂ and 50% Ar, 50% CH₄ atmospheres. The formation of tephroite does not affect the pre-reduction of manganese oxides as, like MnO, the manganese ion is divalent. However, the formation of fayalite may reduce the degree of pre-reduction of iron oxides as it prevents metallic iron formation in some level. Hence, lower silica content or iron of the ore is favorable as they yield less fayalite formation.

Nepheline was identified in all the reduced samples. The EDS mapping of the reduced samples as shown in Figure 10 corroborate the presence of nepheline, as it shows the elements of sodium, aluminum, silicon, and potassium appearing alongside each other. H. Winkler describes a simple production path for nepheline in which a mixture with an approximate composition of Na₂O:Al₂O₃:SiO₂ = 1:1:2 heated to a temperature below 1473 K yielded nepheline [23]. This process is like the calcination process, and it is possible that nepheline be formed. Nepheline was not identified in the calcined XRD pattern, but that might be because of the high levels of noise.

4.3.3. Thermochemistry of the Process

To evaluate the obtained results, thermodynamic calculations were carried out at 1173 K and varying CH_4 amounts to reduce Mn and Fe oxides. Equilibrium diagrams for the reaction up to 4 moles CH_4 with 1 mole Mn_2O_3 and 1 mole Fe_2O_3 at 1173 K were calculated with HSC Chemistry 9, as shown in Figures 11 and 12. The Mn and Fe phases considered in these calculations are Mn_2O_3 , Mn_3O_4 , MnO , Mn , Mn_3C , Mn_5C_2 , Mn_7C_3 , Fe_2O_3 , Fe_3O_4 , FeO , Fe , Fe_3C , Fe_5C_2 , and Fe_7C_3 . These figures show that when the amount of CH_4 in the system is low, CO_2 and H_2O are produced as stable co-existing gases. This is a result of CO and H_2 formation (from the consumed CH_4) and their further interaction to reduce Mn and Fe oxides. When more CH_4 is introduced to the system the concentrations of CO_2 and H_2O are decreased in favor of CO and H_2 gas, indicating that reduction by CH_4 is favored over reduction by CO and H_2 . To reduce 1 mole Mn_2O_3 to 2 moles MnO only considering reduction by CH_4 takes 1 mole CH_4 . The equilibrium diagram in Figure 11 shows that solid carbon is stable when there is more than 1 mole of CH_4 in the system. The equilibrium diagram for Fe in Figure 12 differs from the Mn case. To reduce 1 mole of Fe_2O_3 to 2 moles of Fe only utilizing CH_4 would take 3 moles of CH_4 ; although iron carbides start to form with approximately 2.9 moles of CH_4 in the system. The formation of carbides is indicative of methane cracking. By increasing the CH_4 amount, when all the Fe is converted to carbide, there is a small gap before solid carbon starts to form. The increase in the CH_4 concentration does not cover all the CH_4 that is added to the system. As there is also a drop in the concentrations of CO_2 and H_2O gas it is assumed that with the increased concentration of methane more methane is also used for the reduction to Fe. A drop in the Fe_3C concentration, while the Fe_5C_2 and Fe_7C_3 concentrations increases slightly, is also observed in the gap. This does only seem to be a shift in equilibrium between these phases and not an increase in the overall carbon content.

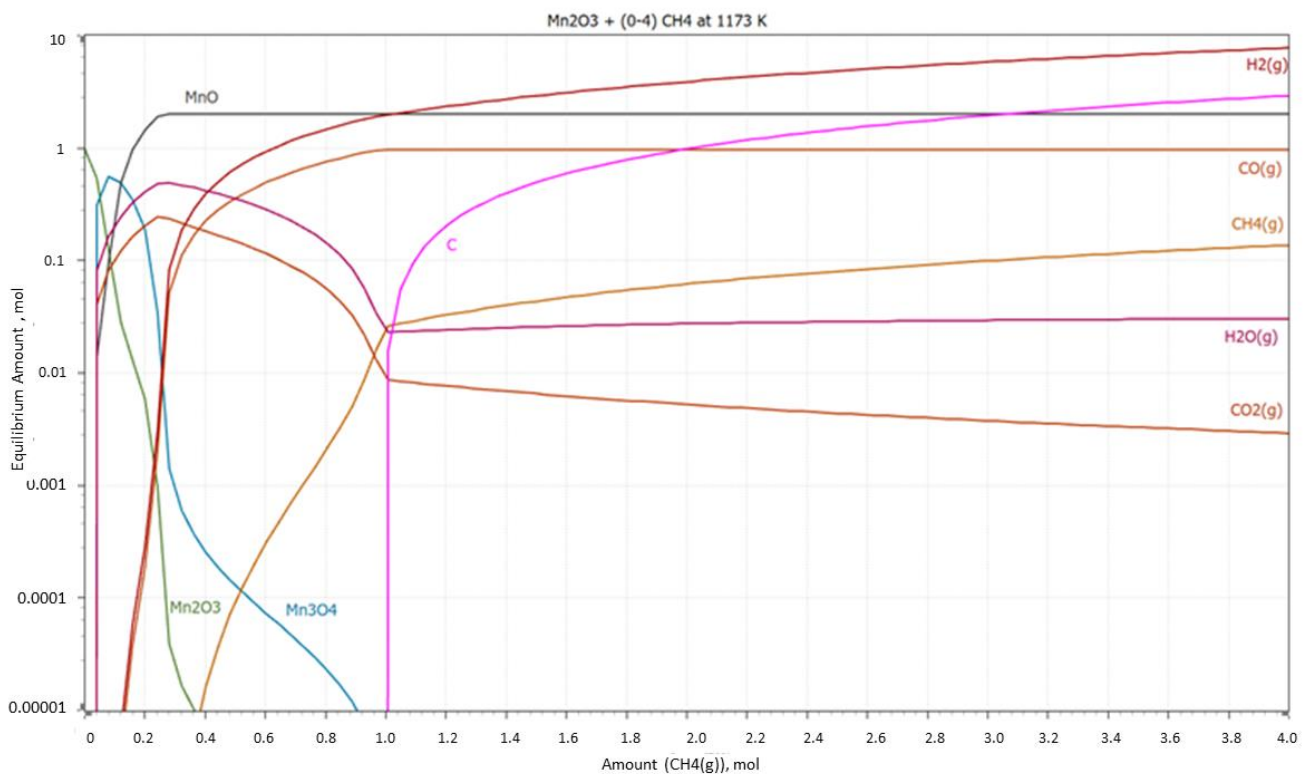


Figure 11. Equilibrium calculations when 1 mole of Mn_2O_3 reacts CH_4 (g) at 1173 K. Created using the equilibrium calculations module in HSC Chemistry 9.

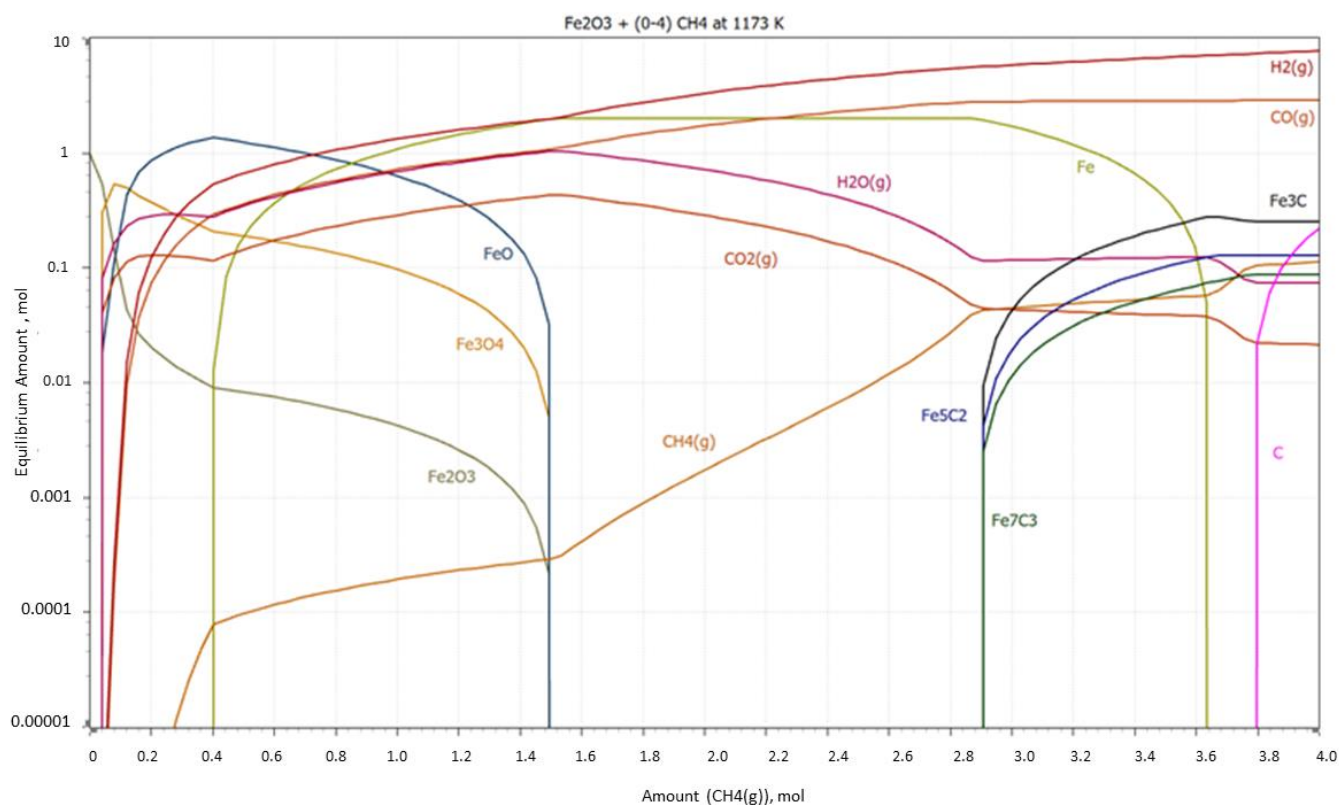


Figure 12. Equilibrium calculations when 1 mole of Fe_2O_3 reacts with CH_4 at 1173 K. Created using the equilibrium calculations module in HSC Chemistry 9.

The equilibrium diagrams do not give information on the kinetics of the systems or how behavior is influenced in a complex system, such as how methane cracking behaves differently in the Mn and Fe systems. For further reduction of MnO, CO has been reported to have a retarding effect [6]. Therefore, an equilibrium diagram with methane as reducing agent does not give a good indication on how MnO will react further. However, the above equilibrium calculations confirm the reduction of the main Fe-containing phases to metallic iron and Mn-containing phases to MnO, which were observed in the reduction experiments in this study.

When methane is used for the reduction of oxides, hydrogen plays a key role in the reduction of oxides as we have methane cracking at elevated temperatures. To evaluate the interaction of PMMN with hydrogen the equilibrium in the system was studied using the XRF analysis data for the calcined ore (Table 2). The obtained result in the case of introducing different amounts of H_2 gas to the system is shown in Figure 13, considering the valuable metals in the ore. It is worth mentioning that no significant changes in the concentration of highly stable oxides (Al_2O_3 , SiO_2 , CaO , MgO) and their phases were observed. Figure 13 shows that MnO_2 is reduced to Mn_2O_3 and Mn_3O_4 with a small amount of H_2 introduction, and these are then converted to MnO. In a similar trend, Fe_2O_3 is converted to Fe_3O_4 , FeO and Fe. However, while FeO content is not changed in a wide range with more H_2 addition, the amount of Fe is increasing and the amounts of Fe_2O_3 and Fe_3O_4 are decreasing. This is in correlation with the concentration changes of H_2 in the system at equilibrium, or in other words, $\text{H}_2/\text{H}_2\text{O}$ ratio. The equilibrium data in Figure 13 indicate that the complete reduction of Cu oxides occurs before the complete reduction of other oxides with hydrogen introduction. A similar behavior is seen for the Co; however, the complete reduction occurs with slightly higher hydrogen introduction. The reduction of NiO is started after complete Co oxide reduction and the majority of NiO is reduced to Ni with slightly more H_2 introduction. Observing the Cu–Ni alloy in the XRD results

above (Figure 8) shows the reduction of Cu and Ni oxides, confirmed by the equilibrium calculations.

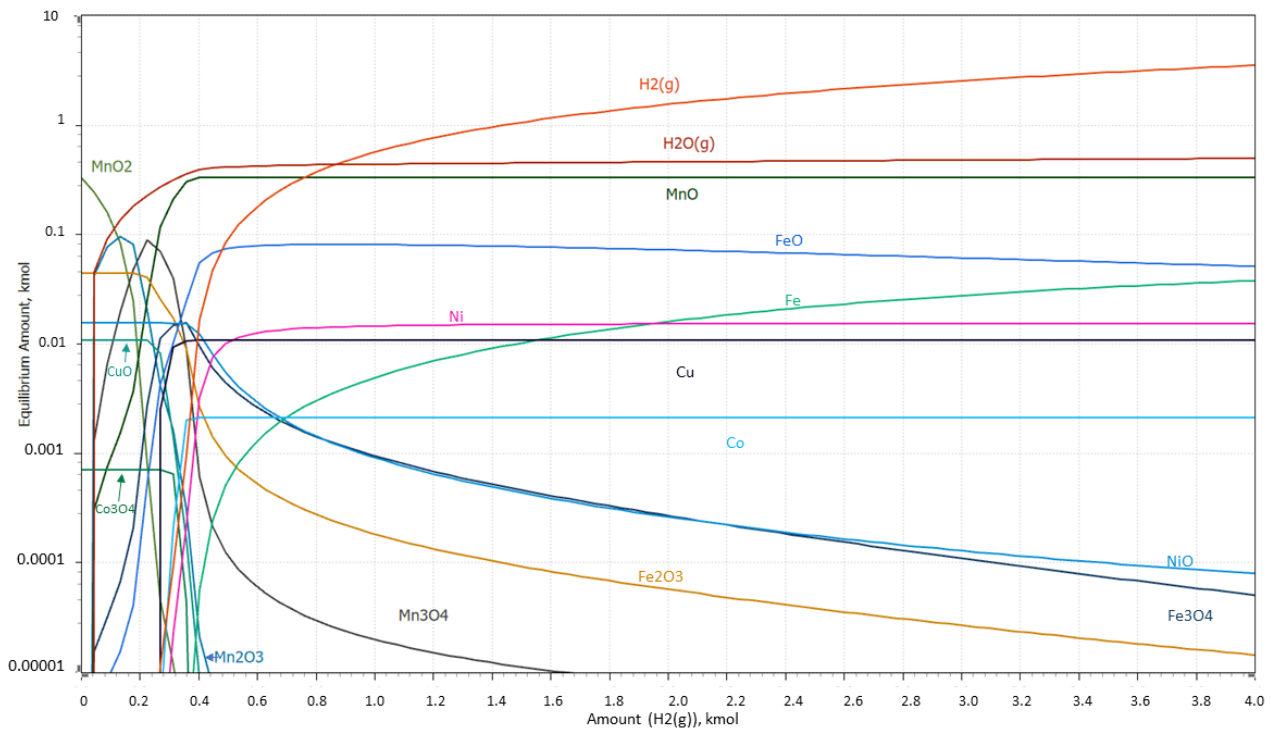
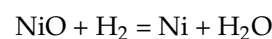
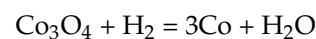
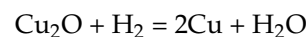
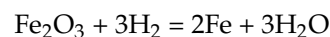
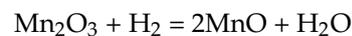


Figure 13. Equilibrium calculations when 100 kg calcined ore reacts with H₂ at 1173 K. Created using the equilibrium calculations module in HSC Chemistry 9.

The equilibrium calculations illustrated in Figure 13 were carried out for a closed system via varying the amount of H₂ gas in the system. In the experiments and in reality, hydrogen or methane are introduced in reduction reactors and the gaseous products, such as H₂O, are taken away, and hence the conditions will be similar to high H₂ quantities in Figure 13, and hence Fe, Cu, Co, Ni and MnO will be the main products. It is emphasized that the Y-axis in Figures 11–13 are in logarithmic scale. Regarding the XRD analysis of the calcined ore that contains Fe₃O₄ (with some Mn₃O₄), Mn₂O₃, Cu₂O, and considering the minor Co₃O₄ and NiO oxides in the ore, the main reduction reactions by hydrogen can be written as follows:



The reduction of the above oxides by CH₄ is complex and has been studied in detail by Cheraghi et al. for Mn and Fe oxides [11]. We did not observe carbon and carbides in our reduced samples; more experimental work is needed to clarify the main reactions involved for the case of using CH₄ and CH₄-H₂ mixtures. Regarding the obtained experimental and modeling results, the recovery of Fe, Cu, Co, and Ni metals is high if a proper separation technique such as smelting is applied, and it may yield an alloy of these metals. Hydrometallurgical processes can be alternatively applied to separate these metals from each other afterwards.

5. Conclusions

In this research, polymetallic manganese nodules were characterized, and their calcination and reduction behavior using H₂ and CH₄ gases and their mixtures were studied. The main conclusions can be summarized as:

- The polymetallic manganese nodules were found to have a highly complex microstructure consisting of several phases.
- In the polymetallic nodules, manganese and iron were found to mostly reside in different phases of lithiophorite (Al_{0.65}H₂Li_{0.33}MnO₄), manganese oxide (MnO₂), vernadite (Mn(OH)₄), chalcophanite (H₆Mn₃O₁₀Zn), and birnessite (MnO₂), and goethite (α-FeO(OH)).
- The valuable Co, Cu, and Ni elements are homogeneously distributed in the main ore components (Fe- and Mn-containing phases) and no known minerals of these metals were found.
- Polymetallic manganese nodules reduction using H₂ and CH₄ and their mixtures yields metallic iron, nickel, copper, and cobalt. While Mn is reduced mostly to MnO state.
- No carbide was found in the samples reduced under methane-containing H₂-CH₄ gas mixtures.
- Silicon content of the ore greatly affected the reduced samples, binding elements of manganese and iron into phases of fayalite and tephroite; they do not affect the pre-reduction extent significantly.
- The silicon contribution in the polymetallic nodules appear to originate from quartz and silicate phases in the nodules.
- The porosity of the manganese nodules during calcination is increased and allows for proper mass transport of reactants and gaseous reduction products.

Author Contributions: Conceptualization, J.S.; methodology, J.S.; software, O.K.B., J.L. and A.H.; validation, J.S.; formal analysis, O.K.B., J.L. and A.H.; investigation, O.K.B. and J.L.; resources, J.S.; data curation, O.K.B. and J.L.; writing—original draft preparation, O.K.B., J.L. and J.S.; writing—review and editing, O.K.B., J.L. and J.S.; visualization, O.K.B. and J.L.; supervision, J.S.; project administration, J.S.; funding acquisition, J.S. All authors have read and agreed to the published version of the manuscript.

Funding: This research received no external funding.

Data Availability Statement: Data are available in a publicly accessible repository that does not issue DOIs.

Acknowledgments: The support from the laboratory staff at the department of Materials Science and Engineering at NTNU is acknowledged.

Conflicts of Interest: The authors declare no conflict of interest.

References

1. Halada, K.; Shimada, M.; Kiyoshi, I. Forecasting of the consumption of metals up to 2050. *J. Jpn. Inst. Metal.* **2007**, *71*, 831–839. [[CrossRef](#)]
2. Monhemius, J. The extractive metallurgy of deep-sea manganese nodules. In *Topics in Non-Ferrous Extractive Metallurgy*, 2nd ed.; Burkin, A.R., Ed.; Blackwell Scientific Publications: Oxford, UK, 1980; pp. 42–69. ISBN 0-632-00648-X.
3. Kuhn, T.; Wegorzewski, A.; Rühlemann, C.; Vink, A. Composition, Formation, and Occurrence of Polymetallic Nodules. In *Deep-Sea Mining*, 1st ed.; Sharma, R., Ed.; Springer: Dona Paula, India, 2017; pp. 23–64.
4. Randhawa, N.; Hait, J.; Jana, R. A brief overview on manganese nodules processing signifying the detail in the Indian context highlighting the international scenario. *Hydrometallurgy* **2016**, *165*, 166–181. [[CrossRef](#)]
5. Agarwal, S.; Jaña, R.; Randhawa, N.; Sahu, K. Carbothermic reduction smelting of manganese nodules to recover valuable metals. In Proceedings of the International Conference on Frontiers of Metallurgy and Materials Technology, Hyderabad, India, 29–31 January 2009.
6. Ochrowicz, K.; Aasly, K.; Kowalczyk, P.B. Recent advancements in metallurgical processing of marine minerals. *Minerals* **2021**, *11*, 1437. [[CrossRef](#)]

7. Drakshayani, D.N.; Sankar, C.; Mallya, R.M. The reduction of manganese nodules by hydrogen. *Thermochim. Acta* **1989**, *144*, 313–328. [[CrossRef](#)]
8. Zhao, F.; Jiang, X.; Wang, S.; Feng, L.; Li, D. The recovery of valuable metals from ocean polymetallic nodules using solid-state metalized reduction technology. *Minerals* **2020**, *10*, 20. [[CrossRef](#)]
9. Sommerfeld, M.; Friedmann, D.; Kuhn, T.; Friedrich, B. “Zero-Waste”: A sustainable approach on pyrometallurgical processing of manganese nodule slags. *Minerals* **2018**, *8*, 544. [[CrossRef](#)]
10. Anacleto, N.; Ostrovski, O.; Ganguly, S. Reduction of Manganese Oxides by Methane-containing Gas. *ISIJ* **2004**, *44*, 1480–1487. [[CrossRef](#)]
11. Cheraghi, A.; Ringdalen, E.; Safarian, J. Kinetics and Mechanism of Low-Grade Manganese Ore Reduction by Natural Gas. *Metall. Mater. Trans. B* **2019**, *50*, 1566–1580. [[CrossRef](#)]
12. Cheraghi, A.; Yoozbashizadeh, H.; Safarian, J. Gaseous Reduction of Manganese Ores: A Review and Theoretical Insight. *Miner. Process. Extr. Metall. Rev.* **2019**, *41*, 198–215. [[CrossRef](#)]
13. Tangstad, M.; Safarian, S.; Bao, S.; Ringdalen, E.; Valderhaug, A. Reaction Rates of $2\text{SiO}_2 + \text{SiC} = 3\text{SiO} + \text{CO}$ in Pellets at Elevated Temperatures. *Asp. Min. Miner. Sci.* **2019**, *3*, AMMS.000558.2019. [[CrossRef](#)]
14. Mindat.org. Available online: <https://www.mindat.org/min-96.html> (accessed on 6 June 2022).
15. Lewis, D.B. Scanning Electron Microscopy and X-ray Microanalysis. *Trans. IMF* **1992**, *70*, 198–202. [[CrossRef](#)]
16. Speakman, S.A. Introduction to X-ray Powder Diffraction Data Analysis. Available online: <http://prism.mit.edu/xray/documents/2%20Introduction%20to%20XRPD%20Data%20Analysis.pdf> (accessed on 6 June 2022).
17. Crum, J.V.; Riley, B.J.; Vienna, J.D. Binary Phase Diagram of the Manganese Oxide-Iron Oxide System. *J. Am. Ceram. Soc.* **2009**, *92*, 2378–2384. [[CrossRef](#)]
18. Coats, A.W.; Redfern, J.P. Thermogravimetric analysis. A review. *Analyst* **1963**, *88*, 906–924. [[CrossRef](#)]
19. Materials Today. Available online: <https://materials-today.com/effect-of-alloying-elements-in-steel/> (accessed on 18 May 2022).
20. Gleeson, B. Thermodynamics and Theory of External and Internal Oxidation of Alloys. In *Shreir's Corrosion*; Cottis, B., Graham, M., Lyon, S., Ruchardson, T., Scantlebury, D., Stott, H., Eds.; Elsevier: Oxford, UK, 2010; pp. 180–194.
21. Barnett, S.J.; Macphee, D.E.; Lachowski, E.E.; Crammond, N.J. XRD, EDX and IR analysis of solid solutions between thaumasite and ettringite. *Cem. Concr. Res.* **2002**, *32*, 719–730. [[CrossRef](#)]
22. Wang, Z.; Peng, B.; Zhang, L.; Zhao, Z.; Liu, D.; Peng, N.; Wang, D.; He, Y.; Liang, Y.; Liu, H. Study on Formation Mechanism of Fayalite (Fe_2SiO_4) by Solid State Reaction in Sintering Process. *JOM* **2017**, *70*, 539–546. [[CrossRef](#)]
23. Winkler, H.G.F. On the synthesis of nepheline. *Am. Mineral.* **1947**, *32*, 131–136.